THE INFLUENCE OF FIN RIGIDITY AND GUSTS ON THE FORCE PRODUCTION IN FISHES AND INSECTS : A COMPUTATIONAL STUDY

Ravi Ramamurti,[*] William C. Sandberg[†] and Rainald Löhner[+]

Naval Research Laboratory, Washington, DC 20375-5344, USA
George Mason University, Fairfax, VA, 22030,USA

ABSTRACT

The three-dimensional unsteady computations of fish swimming with oscillating and deforming fins of varying rigidity were carried out. The objective of these variable rigidity computations was to investigate the importance of fin deformation on the fluid dynamics of force production. An unstructured grid-based unsteady Navier-Stokes solver with automatic adaptive remeshing was used to compute the flow about the wrasse through several complete cycles of pectoral fin oscillation for each of the fins studied. The computations show that when the fin is made rigid by specifying the motion with just the leading edge of the fin tip, the thrust produced during the upstroke is less than half of the peak thrust produced by the flexible cases. During the downstroke, the rigid fin and the fin with the motion prescribed with only the leading and trailing edges produced no positive thrust, while all the flexible cases considered reproduced the thrust production of the fully deformable fin. In the case of the rigid fin, there is a substantial penalty in lift during the upstroke. We have also computed the unsteady flow computations over the *Drosophila* wing with the flight conditions ranging from hovering to a downward gust velocity nearly equal to the mean wing tip velocity. We showed that the wake capture mechanism which is responsible for a peak in thrust production just after stroke reversal diminished with increasing downward velocity and is entirely absent when this velocity reaches the mean wing tip velocity.

INTRODUCTION

Flapping foil propulsion has received considerable attention in the past few years as an alternative to the propeller. This mode of propulsion which involves no body undulation, has many applications, such as submersibles propulsion, maneuvering and flow control which are of interest to the hydrodynamic community and unconventional aerodynamics of Micro Aerial Vehicles (MAV) and the study of aircraft flutter for the aerodynamic community. In order to develop practical MAVs, we have been investigating both fixed wings with propeller driven thrust and flapping wings as a possible propulsive mode. For vehicles with very small inertia, as in the case of MAVs, changes in wing loading can immediately affect the flight path. The need for suppressing the effects of wind gusts becomes important, more so when the airspeed of the vehicle decreases, wind gusts become a large percentage of the mean airspeed of the vehicle. This is further complicated by the fact that the gusts are not always head-on. Since control of these vehicles is one of the most important problems, it is important to suppress unwanted and sudden changes in direction, elevation and orientation.

Flapping foil propulsion is also important in the area of bio-fluid dynamics, for the study of propulsion in insects, birds and certain aquatic animals. Flying animals generate the lift and thrust as a consequence of the interaction of the flapping motions of the wings with the surrounding air. These animals also perform rapid maneuvers involving rapid plunging and pitching motions. Conventional steady state theories are not sufficient to generate enough forces required for flight as shown by Ellington et al. (1996). Therefore, we need to understand the aerodynamics of flapping wings undergoing highly three-dimensional and unsteady motions with varying geometries.

The wing strokes of the insects can be divided into two translational and two rotational phases. During the translational phases, upstroke and downstroke, the wing moves through the air with high angle of attack and during the rotational phases, pronation and supination, the wings rotate rapidly and reverse direction. Dickinson et al. (1999) has studied the effects of the wing rotation in the fruitfly, *Drosophila,* and Walker and Westneat (1997) have studied the kinematics of the fin motion in a class of fishes, namely the bird wrasse, experimentally. Liu and Kawachi (1998) have studied

---

[*] Senior Member, Aerospace Engineer, Code 6410, Laboratory for Computational Physics and Fluid Dynamics.

[†] Deputy Director, Code 6401, Laboratory for Computational Physics and Fluid Dynamics.

[+] Professor, SCS/ Laboratory for Computational Fluid Dynamics.

the flow over a hovering hawkmoth numerically. Ramamurti and Sandberg have studied the force production in *Drosophila* (2002a) and in a swimming bird wrasse fish (2002b) computationally and have shown good agreement with experimental results.

In this study, we seek to complement the experimental studies of Walker and Westneat (1997) on the fin kinematics, center of mass dynamics, and wake visualization by computing the unsteady flow about the bird wrasse *Gomphosus varius* with pectoral fin oscillation and deformation prescribed from the experimental kinematics and Dickinson et al. (1999) on the dynamics of the wing of a hovering *Drosophila*. We continue our earlier computational focus on oscillating control surface flows for non-undulating bodies. The primary objectives in this work, are to (1) investigate the fluid dynamics underlying the generation of forces during pectoral fin oscillation, (2) investigate the effects of varying fin rigidity on the force production and (3) to compare the fluid dynamics of a flapping appendage in gusts with a flapping appendage during hovering.

THE INCOMPRESSIBLE FLOW SOLVER

The governing equations employed are the incompressible Navier-Stokes equations in Arbitrary Lagrangian-Eulerian (ALE) formulation which are written as

$$\frac{d\mathbf{v}}{dt} + \mathbf{v}_a \cdot \nabla \mathbf{v} + \nabla p = \nabla \cdot \sigma, \qquad (1)$$

$$\nabla \cdot \mathbf{v} = 0, \qquad (2)$$

where p denotes the pressure, $\mathbf{v}_a = \mathbf{v} - \mathbf{w}$ the advective velocity vector, where $\mathbf{v}$ is the flow velocity and $\mathbf{w}$ is the mesh velocity and the material derivative is with respect to the mesh velocity $\mathbf{w}$. Both the pressure p and the stress tensor σ have been normalized by the (constant) density ρ and are discretized in time using an implicit time stepping procedure. Thus the equations are Eulerian for zero mesh velocity and Lagrangian if the mesh velocity is the same as the flow velocity. The present time-accurate flow solver is discretized in space using a Galerkin procedure with linear tetrahedral elements. The details of the flow solver have already been discussed extensively elsewhere (Ramamurti *et. al.* 1992, 1994, 1995, 1999) in connection with successfully validated solutions for numerous 2-D and 3-D, laminar and turbulent, steady and unsteady flow problems.

RESULTS AND DISCUSSION

The 3-D surface coordinates of the bird-wrasse, *G. varius*, and the kinematics of the flapping pectoral fin were obtained from Walker and Westneat (1997). In that work, the computations were performed using 14 control points to describe the motion of the deforming fin. The motion of these control points were obtained

from three distal markers and smoothed using a quintic spline function (Walker, 1998). The procedure for using this data in a computational investgation has been described in detail by Ramamurti et al. (2002). In order to carry out computations of the flow about oscillating and deforming geometries, an unstructured mesh with adaptive remeshing is employed. The mesh movement algorithm is briefly summarized here. First, the Cartesian coordinates on the fin surface were then transformed to a parametric space. The coordinates of the surface points were maintained to be constant in the parametric space throughout the computation while the Cartesian coordinates were computed according to the prescribed motion of the control points. Unsteady computations of Ramamurti et al (2002b) about the deforming pectoral fins using this experimentally measured fin kinematics were found to give excellent agreement both in the time history of force production throughout the flapping strokes and also the magnitudes of the generated forces.

In the present work, a set of unsteady computations is carried for several cycles of the fin oscillation for fins of varying rigidity, using the incompressible flow solver described above. By selecting a reduced number of control points the rigidity of the fin is varied. Figure 1 shows the control points along the fin tip at the instant when the fin is fully spread out from the body. All the 14 control points that were supplied from experimental observation are shown in Fig. 1A. Using only one control point at the leading edge of the fin tip and the intersection of the leading and trailing edge rays with the body of the wrasse, we can construct a fin that is rigid, as shown in Fig. 1B. The kinematics of this rigid fin is obtained from the motion of the single control point obtained from the experiments. Using the coordinates of this control point at various instants through the flapping cycle and the location of the root points at the leading and trailing edges, we can obtain the coordinates of the points on the fin tip, so that they lie on a plane. Next, the trailing edge point was added to the list of control points as shown in Fig 1C and another point was added at mid-chord along the fin tip. The resulting initial shape is shown in Fig. 1D. Finally, four control points were chosen out of the original 14, such that the leading edge curvature of the fin is defined properly. The points that were chosen are the leading edge and two successive points close to the leading edge and the trailing edge point. The resulting shape is shown in Fig. 1E.

Unsteady Computations

Bird-Wrasse

Unsteady simulations were carried out with the bird-wrasse swimming at 45 cm/s. The stroke amplitude is approximately 2.14 radians and the frequency of fin

oscillation is 3.3 Hz for all configurations, resulting in a mean tip speed of approximately 50 cm/s. Computations were carried out for more than 4 cycles of fin oscillation using a computational mesh consisting of approximately 150K points and 840K tetrahedral elements, for the four modified fin shapes. The time-varying 3-D lift and thrust, computed by integrating the surface pressure over the wrasse body and fin at each time step throughout the simulation, are shown in Fig. 2.

In the case of the rigid fin, a thrust with a peak value of 0.007 N is produced at the beginning of the downstroke, as shown in Fig. 2A. This is similar to the increase lift just after stroke reversal in the hovering *Drosophila*, reported by Dickinson et al. (1999) and Ramamurti and Sandberg (2002a) and is attributed to the wake capture mechanism. The thrust then quickly drops and a drag force is produced for the remainder of the downstroke. In the case of the flexible fin with two control points, namely the leading and trailing edges of the fin tip, the wake capture peak is absent and no positive thrust is produced during the entire downstroke. In contrast, all the other cases of the flexible fins produce the same thrust during the downstroke as the fully deformable fin with motion prescribed by all14 control points, starting near zero at the beginning of the downstroke and increasing to a maximum of 0.008 N at about 30% of the downstroke. During the upstroke, the rigid fin produces a peak thrust of 0.022 N at about 61% of the upstroke, compared to a peak value of 0.046 N produced by the flexible fin at 64% of the upstroke. The flexible fin with two control points achieves a peak value of 0.046 N but at an earlier time, about 47% of the upstroke. The thrust produced in the case of the flexible fin with three control points is very similar to the fully flexible case. If only the leading edge curvature of the fin is retained, as in the case with 4 control points, the peak thrust achieved during the upstroke is 0.0675 N and occurs at approximately 60% and 92% of the upstroke. It is clear that the results using 3 control points matched exactly with the results obtained using all 14 control points. This is to be expected as the motion of the 14 control points in the experiments were derived from these three points. During the downstroke, the lift, shown in Fig. 2B, produced by the flexible fin using 3, 4 and 14 control points attains a peak value of approximately 0.08 N at 37% of the downstroke; a peak lift of 0.123 N is attained at 30% of downstroke with the leading and trailing edge control points and a maximum lift of 0.16 N is attained at about 40% of the downstroke with a fully rigid fin. But, the rigid fin loses the lift during the upstroke with a minimum lift of –0.37 N at about 50% of the upstroke. The minimum lift attained in the case with 2 control points is approximately –0.145 N, which occurs at about 39% of the upstroke, and for the case

with 4 control points a minimum lift of –0.104 N is attained at about 43% of the upstroke. Again, the case with 3 control points matches exactly with the fully flexible fin, as expected. These results suggest that the fish or a vehicle with a rigid fin or the fin controlled by just 2 points will experience much larger amplitude vertical excursions than with a flexible fin.

Figure 3 shows the pressure distribution on the surface of the Bird-wrasse and its fin at t!= 0.861 s for the fully flexible fin case and the flexible fin with 4 control points. The orientation of the fin in both the cases is nearly the same. The pressure is non-dimensionalized with respect to the dynamic head using the mean tip velocity of 50cm s^{-1}. Comparing Fig. 3B and 3D, we can see that the pressure near the leading edge is higher in the 4 control point case and it extends over a wide region on the upper fin surface. From Figs. 3A and 3C, it is also clear the minimum pressure on the lower surface of the fin is considerably lower (darker blue) in the 4 control point case compared to the fully flexible fin, resulting in a larger thrust force. Figure 4 shows the velocity vectors on a plane $z = 1.5$ cm in the wake of the pectoral fin at t = 0.861 s, which corresponds to nearly the instant at which peak thrust is produced during the upstroke. Although the leading edge curvature is the same in Figs. 4A and 4B, the curvature of the fin in the mid-chord is reduced in the case where only 4 control points were used. This reduces the recirculation both in magnitude and extent on the upper surface of the fin. Hence, the pressure on this surface is higher as shown in Fig. 3D, resulting in a higher thrust.

The increase in thrust production just after the stroke reversal to begin the downstroke, in the rigid fin is investigated next. Figure 5A shows the velocity vectors at an instant where the thrust production reaches a local maximum for the rigid fin. Here, the presence of wake vortices from the previous upstroke in the fin region is clearly evident. These velocity vectors when compared to the case of the fully deformable fin at a similar instant, Fig. 5B, do not show the presence of the upstroke vortices in the fin region. The presence of upstroke vortices also result in an increased pressure, Fig. 5C, near the leading edge approximately 70% of the span away from the root, resulting in an increased thrust at this instant.

Figure 6 shows the orientation of the pectoral fin and the pressure distribution at t = 0.954 s, when the thrust production is minimum for the flexible fin case using 2 control points. At this instant, the pressure distribution on both sides of the fin are shown in Fig. 6A and 6B, for the fully flexible case. Comparing this with the pressure distribution for the case with 2 control point, Figs. 6C and 6D, we see that in both cases, the bottom portion of the fin experiences high pressure near the leading edge. But in the case of the fully flexible fin,

the fin at the leading edge tip is oriented in such a manner so as to produce a thrust. Also, in the case of the fin with 2 control points, a large low pressure region forms near the junction of the fin and the body on the upper surface contributing to a drag. The reason for this low pressure region is due to the presence of a large recirculation region seen in Fig. 7. Although the leading and trailing edges in both case are prescribed in the same manner, the curvature in the 2 control point case, Fig 7B, is pronounced in the middle of the fin compared to the fully flexible case, Fig. 7A, leading to a large recirculation, resulting in lower pressure on the upper surface.

The origin of the loss of lift during the upstroke in the case of the rigid fin is due to the increased angle of attack the fin experiences with respect to the resultant forward velocity of the fish and the velocity of the fin. In the case of the fully flexible fin, the fin is flexed concave upwards reducing the angle of attack at the leading edge whereas the flow is directly incident on the upper surface of the rigid fin. This is clear from the pressure distribution on the rigid fin at t= 0.855 s, Fig. 8D and 8E, compared to that of the fully flexible case at a close instant, Figs. 8A and 8B. In both cases, a high pressure region is formed at the leading edge of the fin tip on the upper surface of the fin and lower pressure on the bottom surface, contributing to a downward force. But, the magnitudes of these pressures are much higher in the rigid case, thus producing a large downward force. In the case of the fully flexible fin, this loss of lift is offset by the upward force in the region close to the body where high pressure exists on the bottom surface and lower pressure on the upper surface. The lower pressure on the upper surface appears due to the presence of a recirculation region at the body junction, shown in Fig. 8C which is absent in the rigid case, Fig. 8F due to the lack of curvature of the fin. Figure 9 shows the pressure distribution on the fully flexible fin (A and B) and the rigid fin (C and D) at an instant close to the maximum lift production during the downstroke. Again, the lower side of the fin has higher pressure with the rigid fin experiencing larger magnitude of pressure difference, producing a larger lift.

Drosophila

The configuration of the hovering *Drosophila melanogaster* is shown in Fig. 10A. The coordinate system (x,y,z) is fixed to the body with the x coordinate normal to the stroke plane. During the translational phases (upstroke and downstroke) the wing moves from close to the y axis through an angle ϕ, the wingbeat amplitude. The flapping wing configuration used in the flow simulations is shown in Fig. 10B. This is based on the experimental arrangement of Dickinson *et al.* (1999) and is also described by Ramamurti and Sandberg (2002). The planform of the wing is derived

from the *Drosophila* wing and is 25 cm long and 3.2 mm thick. Fig. 10B shows the position of the wing at three different times during the flapping cycle. The upward gust velocity **V** is varied from a hovering condition of zero to the mean tip velocity of the flapping wing. The mean wing-tip velocity is defined as, $U_t = 2\phi nR$, where R is the wing length (25 cm), n is the frequency of flapping motion (0.145 Hz), and ϕ is the wingbeat amplitude (peak to peak, 2.79 radians).

The flow solver described above was used to compute the flow past the *Drosophila* wing undergoing rotation and translation. First, an inviscid solution was obtained using a grid consisting of 178,219 points and 965,877 tetrahedral elements. The unsteady solution was carried out for 5 cycles of oscillation of the wing using prescribed kinematics. The kinematics of the wing is given in detail by Ramamurti and Sandberg (2002a). The surface pressure on the wing is integrated to obtain the forces on the wing along the three axes (F_x, F_y, F_z). The thrust T and the drag D forces are then computed as, $T = -F_x$ and $D = \sqrt{(F_y^2 + F_z^2)}$, respectively. These forces were nondimensionalized as follows:

$$C_T = \frac{T}{\frac{1}{2}\rho U_t^2 \bar{c} R r_2^2(s)} \quad \text{and}$$

$$C_D = \frac{D}{\frac{1}{2}\rho U_t^2 \bar{c} R r_2^2(s)} , \tag{3}$$

where ρ is the density of the mineral oil (880 Kg m^{-3}), U_t is the mean wing-tip velocity, $r_2^2(s)$ is the second moment of the area (0.4), $\bar{c} = 2R/AR$ and AR is the aspect ratio of the wing.

The downward gust velocity is then increased from a hovering condition to the mean wing tip velocity and the unsteady computations are performed. Figure 11 shows the time history of the thrust and drag forces during one cycle of the wingbeat for the various gust velocities considered. The coefficient of thrust (C_T) achieves a maximum just prior to the stroke reversal (Fig 11A). For a hovering case, this peak value is 2.05 and as the downward velocity is increased the magnitude of this peak diminishes to 1.15 for the maximum downward velocity (**V** = 20 cm s^{-1}) considered. This effect is expected as this peak is mainly due to the rotational effect of the wing, which is rotating in a counterclockwise direction about the y-axis at the beginning of the downstroke. A downward velocity in the x-direction will diminish the Magnus effect which produces the lift and hence the peak thrust is reduced. This rotational effect is also responsible for the increase in drag coefficient prior to stroke reversal seen in Fig 11B. These rotation effect peaks also shift

closer to the stroke reversal as the velocity is increased. From Fig 11A, it is clear that a peak thrust is produced just after the stroke reversal. This peak is attributed to the wake capture effect, in which the wing passes through the shed vorticity of the previous stroke. Figure 12 shows the velocity vectors on a plane $y = 10$cm at the beginning of the downstroke. For symmetric rotation, the wing chord is aligned with the x-axis at the beginning of the stroke reversal. For the hovering case, a vortex is seen near the leading edge on the bottom surface of the wing. This vortex was shed during the previous upstroke. As the downward gust velocity is increased the strength of this vortex reduces in strength and disappears entirely at a velocity $\mathbf{V} = 20$ cm s^{-1}. This is due to the fact that the effective angle of attack (α) of the wing with respect to the combined velocity vector of the translational and downward velocity is reduced as the gust velocity is increased. Figure 13 shows the vorticity contours in the spanwise direction on a plane $z' = 10$cm from the center of rotation. It is clear from Fig. 15A that the leading edge vortex is formed during the upstroke in the hovering case.

SUMMARY AND CONCLUSIONS

We computed the unsteady dynamics about a bird wrasse with flapping and deforming pectoral fins using a new moving mesh capability for unstructured adaptive meshes. The unsteady computations using the prescribed kinematics of the pectoral fin have been compared experimental results. By selecting a reduced number of control points used to define the fin kinematics, the rigidity of the fin was varied. Several unsteady computations were performed fro various rigidity of the fin ranging from a fully rigid to a fully deformable fin. We found that when the fin is made rigid by specifying the motion with just the leading edge of the fin tip, the thrust produced during the upstroke is less than half of the peak thrust produced by the flexible cases. During the downstroke, the rigid fin and the fin with the motion prescribed with only the leading and trailing edges produced no positive thrust. All the flexible cases reproduced the thrust production of the fully deformable fin. In the case of the rigid fin, a wake capture mechanism was observed that resulted in a small thrust increase just after the beginning of the downstroke. During the upstroke, when only the leading edge curvature is prescribed, as in the case with 4 control points, the peak thrust exceeds the fully deformable fin. Although the leading edge curvature was maintained to be the same between the 4 control point case and the fully deformable fin, the curvature in the mid chord region is much reduced when only the leading edge curvature is specified. This led to a smaller recirculation region on the upper surface of the fin producing extra thrust. From the point of view of lift production, we found that all of the cases with flexible fins performed in a similar manner except the fin controlled by just the leading and trailing edge points. In the case of the rigid fin, there was a substantial loss of lift during the upstroke. Therefore, the fish or a vehicle with rigid fin or a fin controlled by just the leading and trailing edge points would experience much more vertical excursions that one with a flexible fin.

We have also performed unsteady flow computations over the *Drosophila* wing with the flight conditions ranging from hovering to a downward gust velocity nearly equal to the mean wing tip velocity. The effect of this downward velocity is a reduction in the rotational forces that produces a peak in the thrust and drag just prior to stroke reversal. We showed that the wake capture mechanism which is responsible for a peak in thrust production just after stroke reversal diminished with increasing downward velocity and is entirely absent when this velocity reaches the mean wing tip velocity.

REFERENCES

Dickinson, M. H., Lehmann, F.-O. and Sane, S. P. (1999). Wing rotation and the aerodynamic basis of insect flight. *Science* **284**, 1954-1960.

Ellington, C. P., Van den Berg, C. and Willmott, A. P. (1996). Leading-edge vortices in insect flight. *Nature* **384**, 626-630.

Liu, H. and Kawachi, K. (1998). A numerical study of insect flight. *J. comp. Physics*. **146**, 124-156.

Ramamurti, R. and Löhner, R. (1992). Evaluation of an Incompressible Flow Solver Based on Simple Elements, *Advances in Finite Element Analysis in Fluid Dynamics*, FED **137**, Editors: Dhaubhadel, M. N. *et al.*, ASME Publication, New York, 33-42.

Ramamurti, R. and Sandberg, W.C. (2002a). A Three-Dimensional Computational Study of the Aerodynamic Mechanisms of Insect Flight**,** *J. Exp. Biol*. **205**, 1507-1518.

Ramamurti, R., Löhner, R., and Sandberg, W. C. (1994). Evaluation of a Scalable 3-D Incompressible Finite Element Solver, *AIAA-94-0756*, Washington, DC.

Ramamurti, R., Löhner, R., and Sandberg, W. C. (1995). Simulation of a Torpedo Launch Using a 3-

D Incompressible Finite Element Flow Solver, *AIAA-95-0086*, Washington, DC.

Ramamurti, R., Löhner, R., and Sandberg, W. C. (1999). Computation of the 3-D Unsteady Flow Past Deforming Geometries, *Int. J. Comp. Fluid Dyn.*, 13, 83-99.

Ramamurti, R., Sandberg, W.C. and Löhner, R. (2000). Simulation of the Dynamics of Micro Air Vehicles, *AIAA-2000-0896*, Reno, NV.

Ramamurti, R., Sandberg, W.C., Löhner, R., Walker, J. A. and Westneat, M. W. (2002b). Fluid Dynamics of Flapping Aquatic Flight in the Bird Wrasse: 3-D Unsteady Computations with Fin Deformation, *J. Exp. Biol.* **205**, 19, 2997-3008.

Walker, J. A. and Westneat, M. W. (1997). Labriform Propulsion in Fishes: Kinematics of Flapping Aquatic Flight in the Bird Wrasse, *Gomphosus Varius*. (Labridae), *J. Exp. Biol.* **200**, 1549-1569.
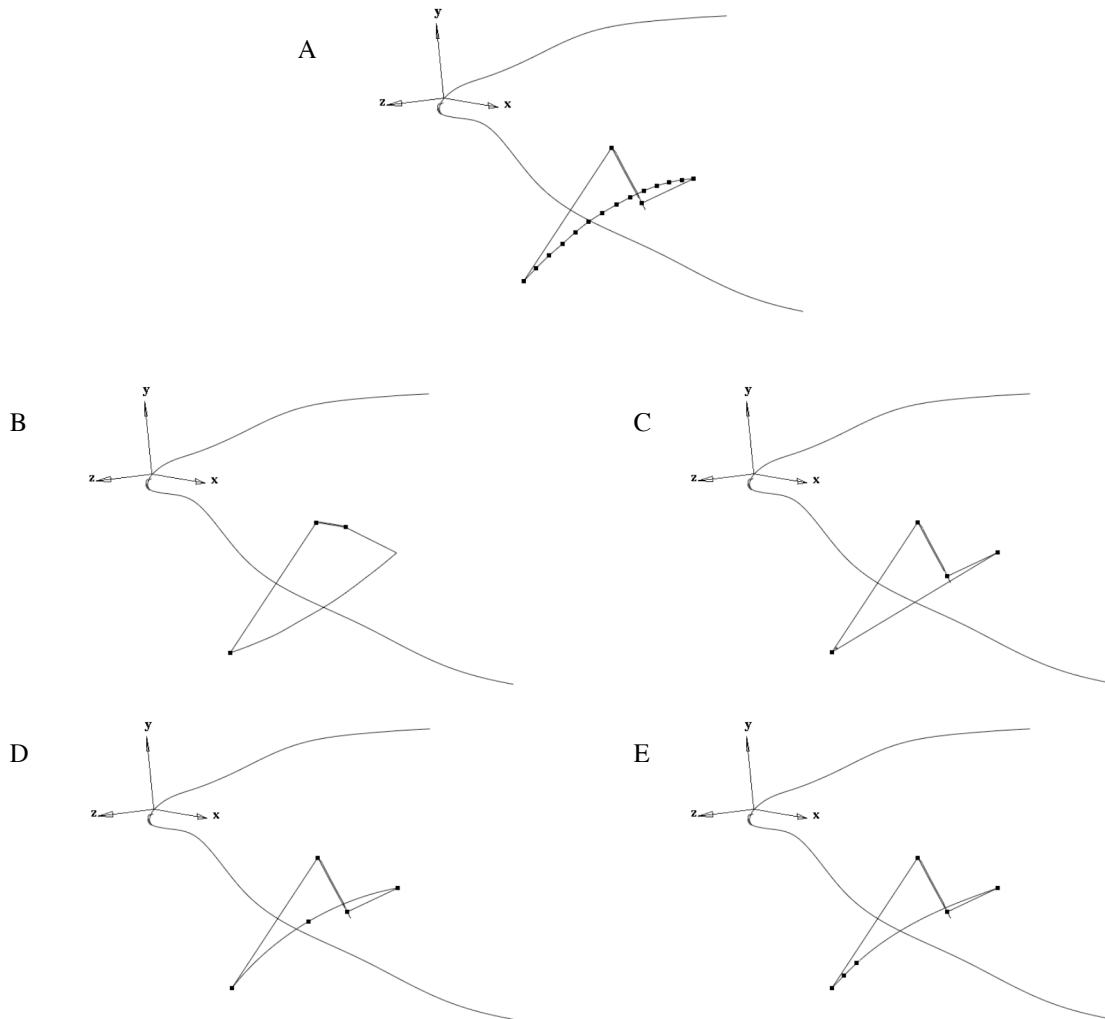
Fig. 1. Shapes of the fully deformable Bird-wrasse fin and modified fin at an instant when the fin is fully extended. (A) The experimentally observed deformable fin with 14 control points, (B) modified rigid fin with a control point on the leading edge and at the tip of the fin, (C) flexible fin with control points at the leading and trailing edges of the fin tip, (D) flexible fin with 3 control points, and (E) flexible fin with 4 control points closer to the leading edge.
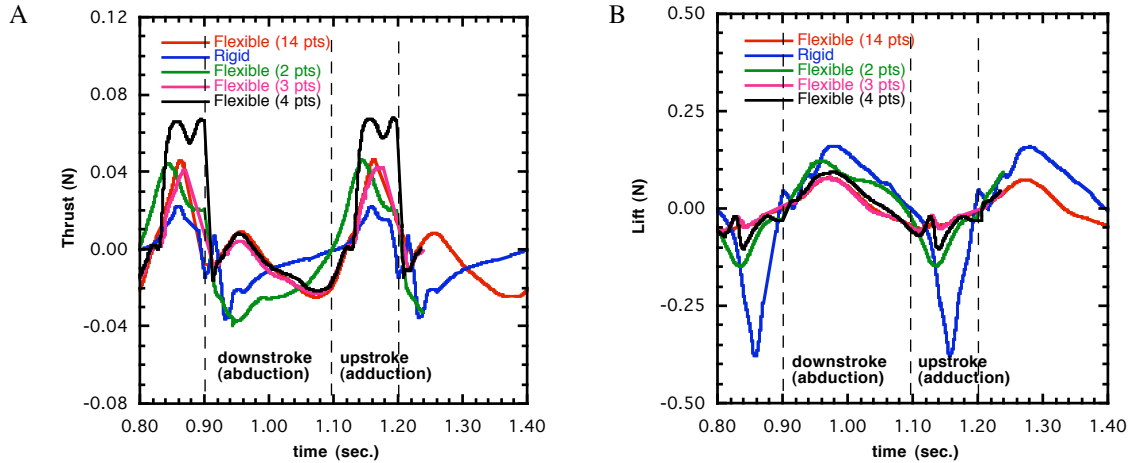
Fig. 2. Effect of fin flexibility on the time variation of (A) thrust and (B) lift forces.
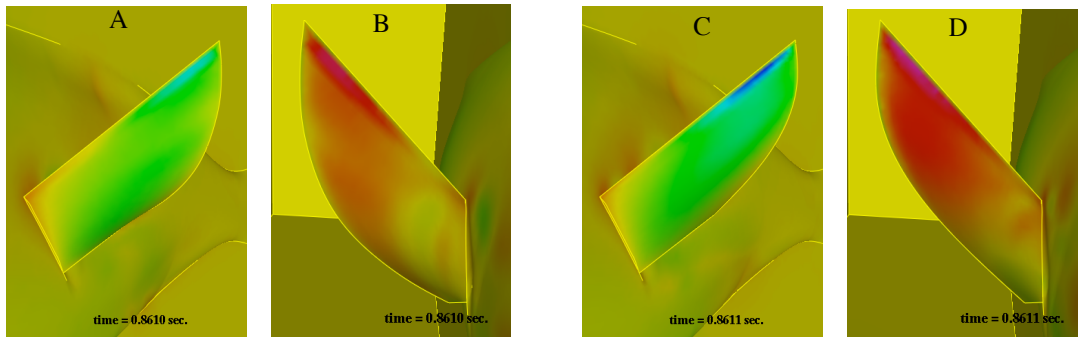
Fig. 3. Surface pressure distribution on the Bird-wrasse at an instant when the thrust is maximum during the upstroke. The pressure is non-dimensionalized with respect to the dynamic head of the mean tip velocity. (A, B) 14 control points were used to define the kinematics of the fin. (A) view from the front of the lower side of the fin. (B) view from the back of the fin. (C, D) 4 control points were used to define the kinematics of the fin. (C) view from the front of the lower side shows lower pressure compared to (A) and (D) view from the back of the upper side of the fin show higher pressure compared to (B), resulting in a higher thrust.
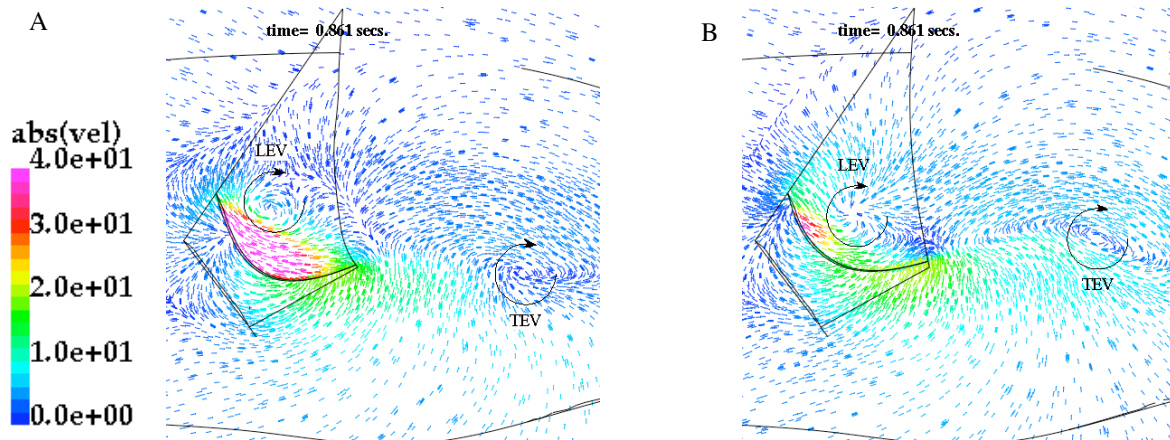
Fig. 4. Velocity vectors on a plane $z = 1.5$ cm at an instant $t = 0.861$ s, when the thrust production is maximum during the upstroke with fin kinematics prescribed with (A) 14 control points and (B) with 4 control points. The swimming velocity of the fish (45 cm!s^{-1}) is subtracted from the x component of the velocity and only the in-plane components are shown to reveal the vortical structures. LEV, leading edge vortex; TEV, trailing edge vortex.

7
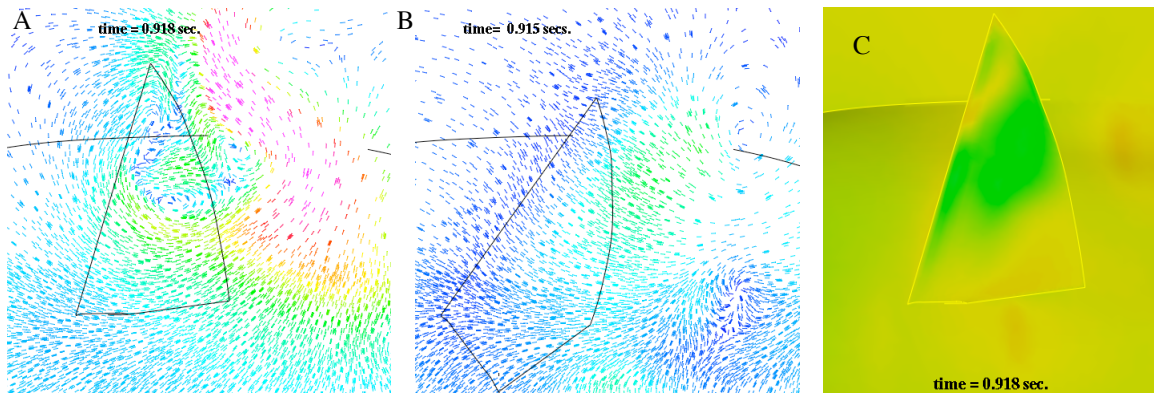
Fig. 5. Thrust production in the rigid fin just after stroke reversal, $t = 0.918$ s. (A) velocity vecors on a plane $z = 1.5$ cm, show vortices from the wake of the previous upstroke, (B) velocity vectors just after stroke reversal for the fully deformable fin showing the absence of the vortices in the fin region, and (C) pressure distribution on the lower side of the rigid fin showing higher pressure region due to the presence of the wake vortices.
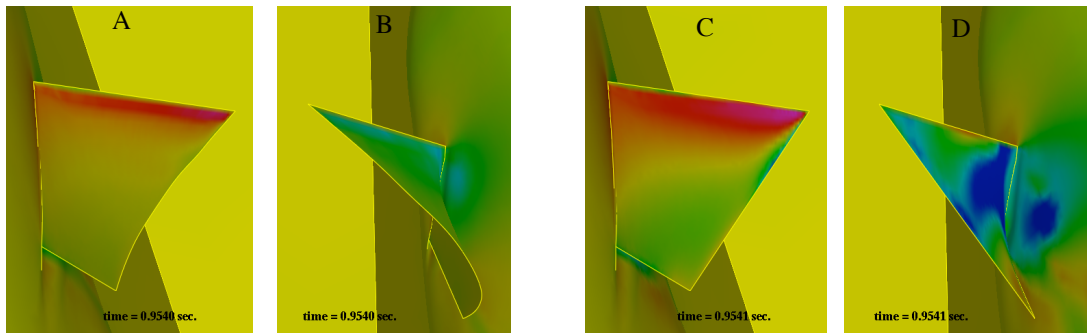

Fig. 6. Pressure distribution on the Bird-wrasse and its pectoral fin at $t = 0.954$ s during the downstroke, (A, B) when the thrust reaches maximum for the fully flexible fin and (C, D) when the thrust reaches a minimum for case with the fin kinematics prescribed by 2 control points.
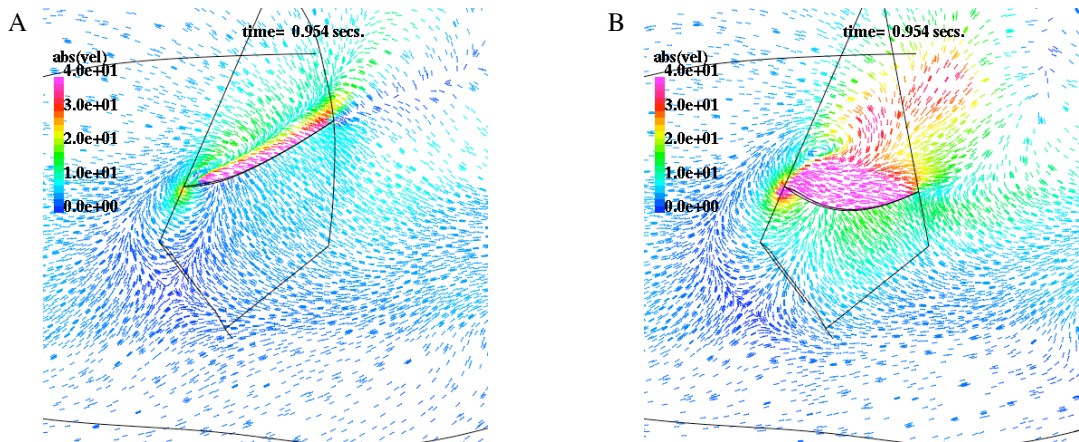
Fig. 7. Velocity vectors on a plane $z = 1.5$ cm at an instant $t = 0.954$ s, (A) when the thrust production is maximum during the downstroke with fin kinematics prescribed with 14 control points and (B) when the thrust production reaches a minimum with 2 control points.
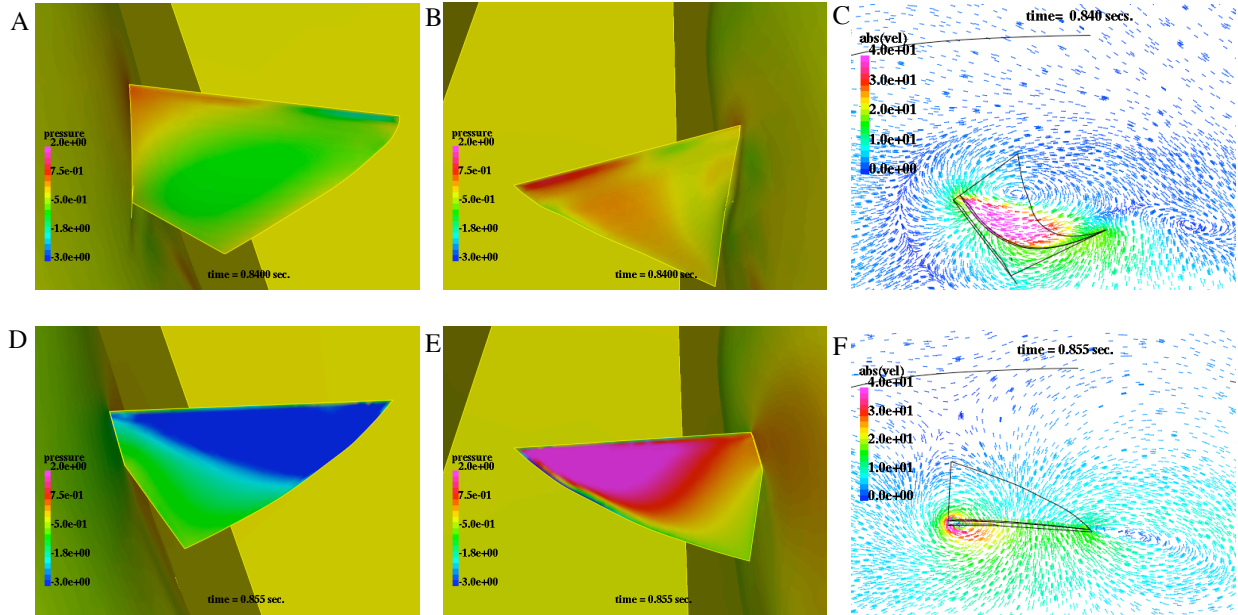
Fig. 8. Surface pressure contours on the pectoral fin and velocity vectors on a plane z = 1.5 cm at an instant when the lift is minimum during the upstroke for the rigid fin. (A-C) fully flexible fin; (D-F) rigid fin. Pressure distribution on the lower surface viewed from the bottom(A, D) and on the upper surface viewed from the top (B, E). (C) Velocity vectors show a large recirculation on the upper surface, lowering the pressure and thus increasing lift when compared to (F) a fully attached flow in the rigid case.
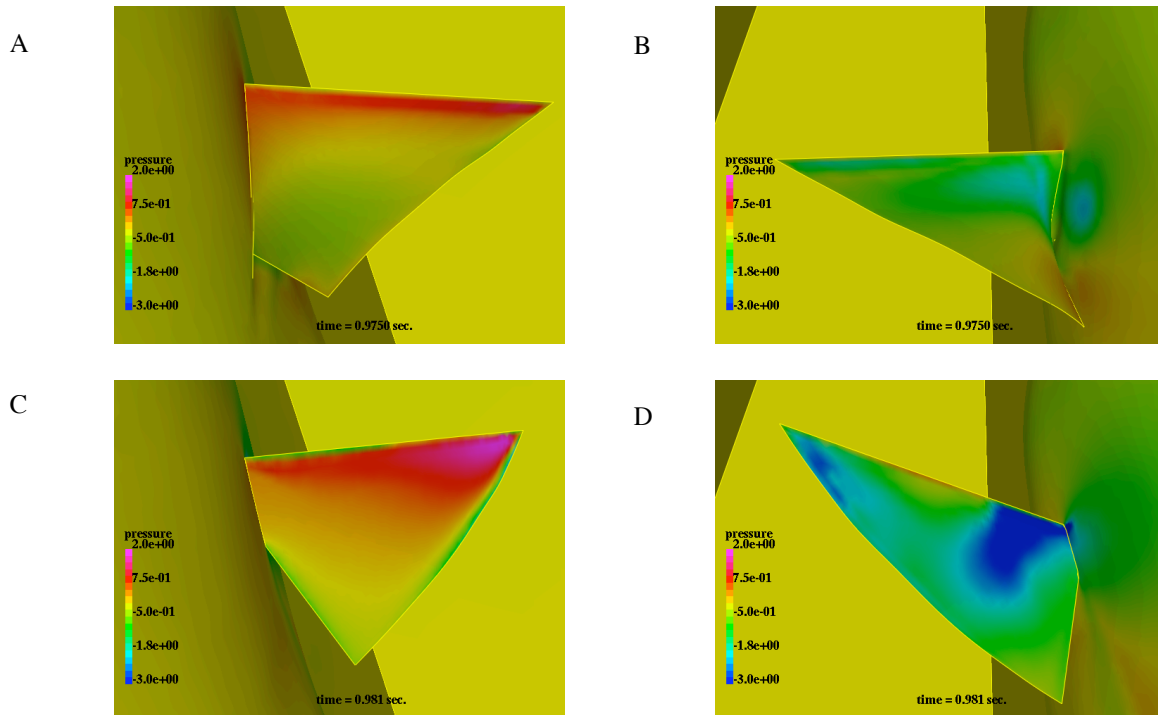
Fig. 9. Surface pressure distribution on the pectoral fin at an instant when the lift is near maximum during the downstroke, (A, B) for the fully flexible fin and (C, D) for the rigid fin. (C) Lower surface of the fin viewed from the bottom shows higher pressure at the distal edge of the fin and most of the lower surface when compared to (A) and the pressure on the upper surface is much lower for the rigid case (D) when compared to the fully flexible fin (B), resulting in a higher lift force.

9
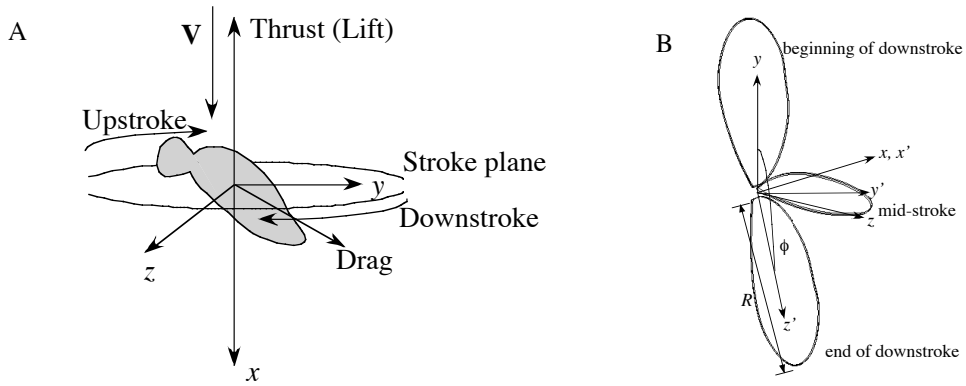
Fig. 10. (A) Schematic of a hovering *Drosophila* showing the orientation of the *x,y,z* coordinate system and the direction of the gust velocity **V**. (B) Schematic diagram of the flapping Drosophila wing. The position of the wing is shown at three different times during the flapping cycle. The coordinate system (x',y',z') is fixed to the wing, and the wing rotates about the z' axis throughout the cycle. *R,* wing length; ϕ wingbeat amplitude.
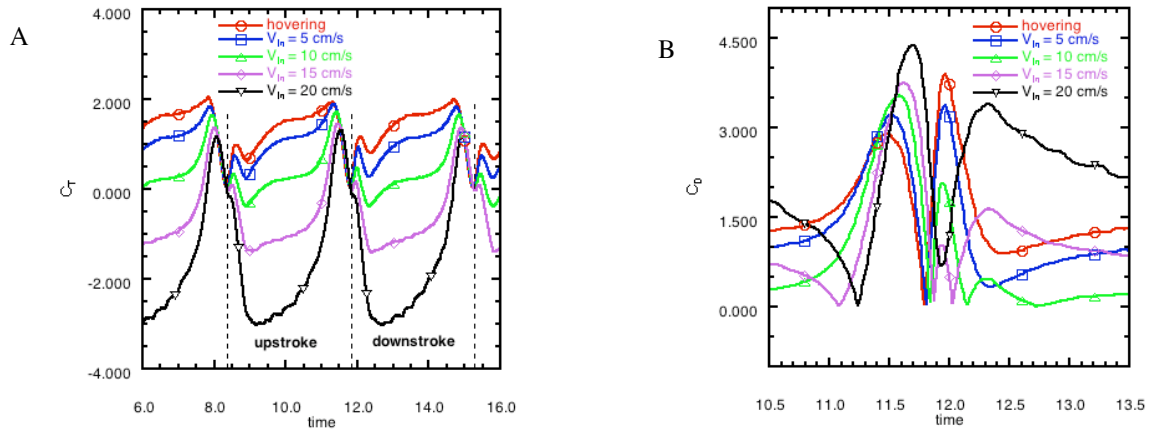

Fig. 11. Time Variation of (A) the thrust coefficient through one cycle of flapping and (B) drag coefficient near the beginning of the downstroke.
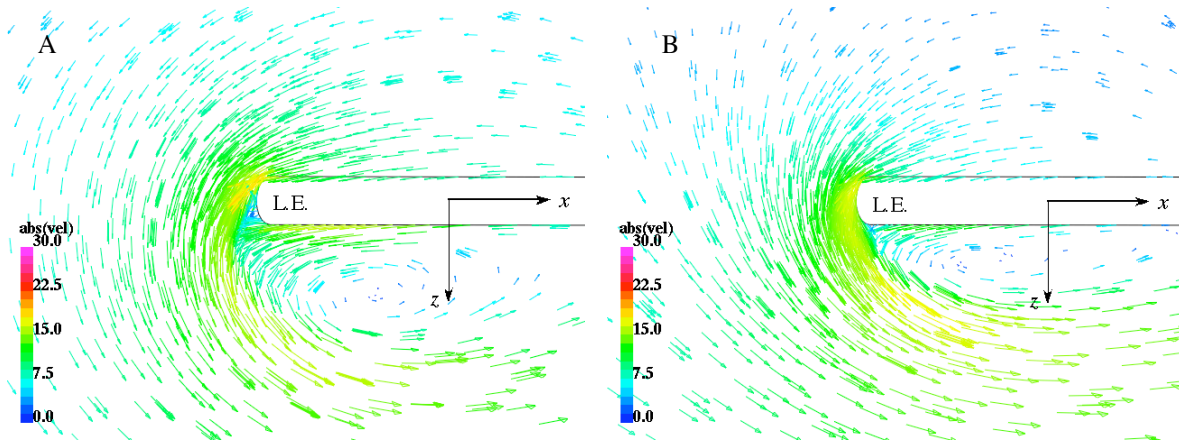

Fig. 12. Velocity vectors at the beginning of the downstroke at t = 11.81 s. (A) A large vortex shed from the previous upstroke is seen near the leading edge (L.E.) in hovering, (B) and is smaller for **V** = 5 cm s⁻¹.

10
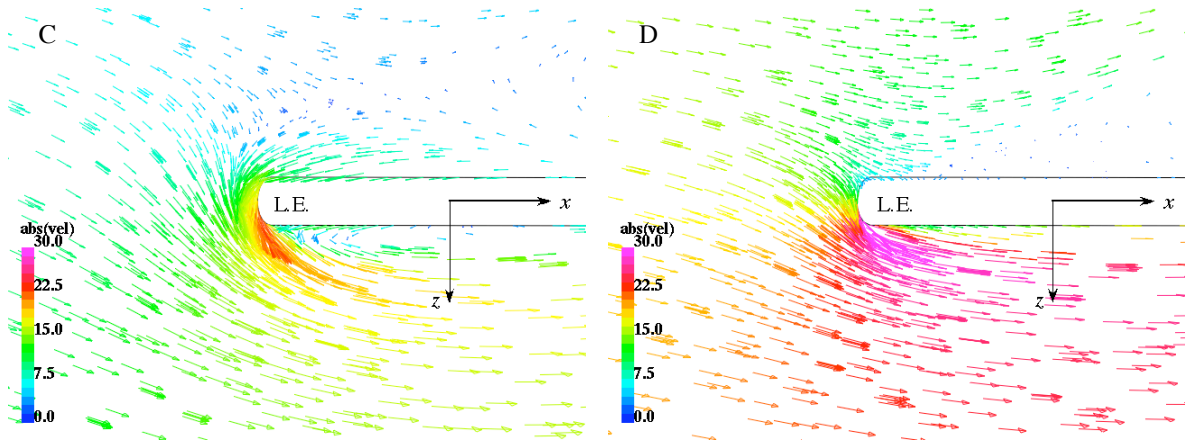
Fig. 12 (cont'd.) Velocity vectors at the beginning of the downstroke at t = 11.81 s. (C) reduces further in size for **V** = 10 cm s^{-1} and (D) is absent for **V** = 20 cm s^{-1}.
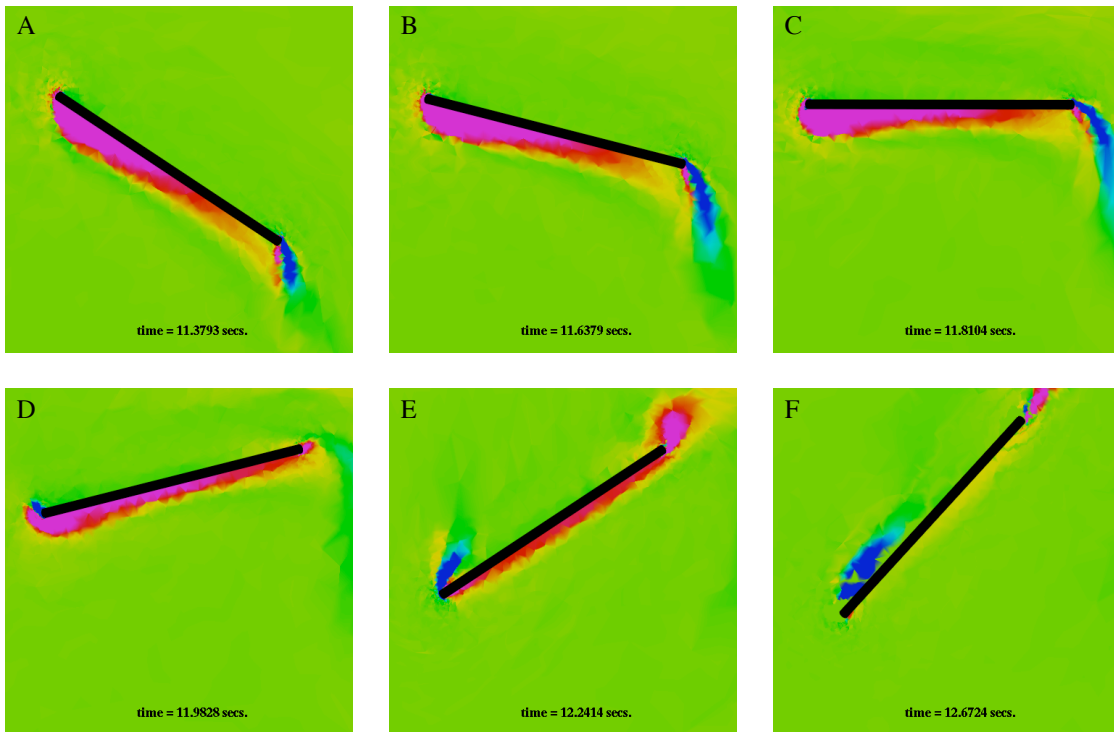

Fig. 13. Vorticity contours on a plane $z' = 10$cm during stroke reversal. Before stroke reversal (A, B), a leading edge vortex is seen on the bottom surface of the wing and continues to be present at stroke reversal (C) and beyond (D). At t = 12.24 s, this leading vortex from the previous upstoke disappears completely (E) and a vortex on the upper side of the wing begins to form (F).